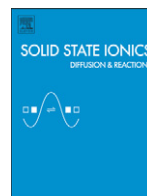




Contents lists available at SciVerse ScienceDirect

Solid State Ionics

journal homepage: [www.elsevier.com/locate/ssi](http://www.elsevier.com/locate/ssi)

## *In situ* X-ray diffraction study of the lithium excess layered oxide compound $\text{Li}[\text{Li}_{0.2}\text{Ni}_{0.2}\text{Mn}_{0.6}]\text{O}_2$ during electrochemical cycling <sup>☆</sup>

Christopher R. Fell <sup>a</sup>, Miaofang Chi <sup>b</sup>, Ying Shirley Meng <sup>a,c</sup>, Jacob L. Jones <sup>a,\*</sup><sup>a</sup> Department of Materials Science and Engineering, University of Florida, Gainesville, FL 32611, United States<sup>b</sup> Materials Science and Technology Division, Oak Ridge National Laboratory, Oak Ridge, TN 37831, United States<sup>c</sup> Department of NanoEngineering, University of California San Diego, La Jolla, CA 92037, United States

## ARTICLE INFO

## Article history:

Received 7 July 2011

Received in revised form 3 November 2011

Accepted 21 November 2011

Available online xxxxx

## Keywords:

Lithium ion battery

*In situ* X-ray diffraction

Cathode

## ABSTRACT

*In situ* X-ray diffraction patterns were collected using a laboratory X-ray diffractometer during the first electrochemical charge/discharge cycle of the layered lithium excess compound  $\text{Li}[\text{Li}_{0.2}\text{Ni}_{0.2}\text{Mn}_{0.6}]\text{O}_2$  in the family of  $\text{Li}[\text{Ni}_x\text{Li}_{1/3-2x/3}\text{Mn}_{2/3-x/3}]\text{O}_2$  ( $x = 1/5$ ). Dynamic changes in peak positions, lattice parameters, and micro-strain help to explain the lithium de-intercalation mechanism in this class of materials. Strong anisotropy is observed in the shifts of the lattice parameters during the first cycle. The *in situ* electrochemical measurement shows dynamically changing strain during the first electrochemical cycle that is explained by known lithium and transition metal (TM) migration mechanisms.

Published by Elsevier B.V.

## 1. Introduction

The lithium-excess layered oxide compounds  $\text{Li}[\text{Ni}_x\text{Li}_{1/3-2x/3}\text{Mn}_{2/3-x/3}]\text{O}_2$  ( $0 < x < 1/2$ ) are of great interest as a new generation of positive electrode materials for high energy density lithium-ion batteries because of their high energy density at lower costs. These layered structures are derived from  $\text{LiCoO}_2$ ; however, the additional  $\text{Li}^+$  present in the transition metal (TM) layers induce cation ordering in the TM layers [1,2]. The X-ray diffraction pattern of the  $\text{Li}[\text{Ni}_x\text{Li}_{1/3-2x/3}\text{Mn}_{2/3-x/3}]\text{O}_2$  ( $0 < x < 1/2$ ) series of materials can be refined with the  $\alpha\text{-NaFeO}_2$  structure (R3m) with the exception of the superlattice peaks between  $20$  and  $35^\circ 2\theta$ , which are associated with a honeycomb ordering of  $\text{Li}^+$ ,  $\text{Ni}^{2+}$  and  $\text{Mn}^{4+}$  in the transition metal layer consistent with the  $\text{Li}_2\text{MnO}_3$ -honeycomb type ordering [3,4]. This material family can be viewed as a solid solution between the two components,  $\text{Li}_2\text{MnO}_3$  ( $x = 0$ ) and  $\text{Li}[\text{Ni}_{1/2}\text{Mn}_{1/2}]\text{O}_2$  ( $x = 1/2$ ) [5], in which Ni is  $2+$  and Mn is  $4+$ . It has been shown that upon lithium removal,  $\text{Ni}^{2+}$  is oxidized to  $\text{Ni}^{4+}$  and  $\text{Mn}^{4+}$  remains unchanged up to  $4.40\text{ V}$  [5–7]. However, the total amount of Li extracted from the material, particularly in the first charge cycle, is much larger than the theoretical capacity calculated from the  $\text{Ni}^{2+}/\text{Ni}^{4+}$  redox couple. Deintercalation of Li from the material, when both Ni and Mn are in their fully charged ( $4+$ ) oxidation states, is associated with a well defined plateau region near  $4.5\text{ V}$  [2,8–10].

Significant efforts have been devoted to explain the anomalous capacity from the plateau region; possible causes are irreversible loss of oxygen, electrode/electrolyte reactions and/or hydrogen exchange [2,9,11]. Although the source of the behavior is still under debate, previous work has shown clear evidence that after electrochemical cycling to  $4.8\text{ V}$ , Li/Mn honeycomb-type ordering disappears indicating significant cation migration [11–13].

There have been great efforts to observe the detailed structural changes that occur in the bulk and at the surface of the layered Li excess family of materials during the charging and discharging processes. The advantage of *in situ* X-ray diffraction lies in the ability to directly monitor detailed structural changes in the electrode material as Li extraction/insertion proceeds. The *in situ* X-ray measurement, combined with electrochemical measurements provides valuable information about the relationship between structure and electrochemical properties which is not obtainable from *ex situ* structural measurements [2,14–16]. The layered Li excess compounds have not been extensively studied using *in situ* X-ray diffraction. Previous experiments by Lu and Dahn have explored changes in volume and lattice parameters showing the collapse in the  $c$  lattice parameter during the first charge cycle leading to a modified structure following the first discharge cycle [2]. However, use of peak profile analysis to reveal the microstructure change of these materials has not been quantitatively done. In this paper we apply a combination of *in situ* X-ray diffraction, using an X-ray laboratory diffractometer, and *ex situ* transmission electron microscopy to examine the  $\text{LiNi}_{0.2}\text{Li}_{0.2}\text{Mn}_{0.6}\text{O}_2$  electrode material to probe changes of the structure during the first charge and discharge cycle. These changes are linked to the structural model to illustrate significant strain contributions developing during the first electrochemical cycle profile.

<sup>☆</sup> Edited by Christopher Fell June 24, 2011

\* Corresponding author.

E-mail addresses: [fellc@ufl.edu](mailto:fellc@ufl.edu) (C.R. Fell), [jjones@mse.ufl.edu](mailto:jjones@mse.ufl.edu) (J.L. Jones).

## 2. Experimental method

### 2.1. Sample synthesis and preparation

$\text{Li}[\text{Ni}_x\text{Li}_{1/3-2x/3}\text{Mn}_{2/3-x/3}]\text{O}_2$  ( $x = 1/5$ ) powders were prepared by the mixed hydroxide method as previously explained in Ref. [13]. Transition metal nitrates,  $\text{Ni}(\text{NO}_3)_2 \cdot 6\text{H}_2\text{O}$  and  $\text{Mn}(\text{NO}_3)_2 \cdot 4\text{H}_2\text{O}$  were titrated into a  $\text{LiOH} \cdot \text{H}_2\text{O}$  solution for a duration of 2 h. The coprecipitated transition metal hydroxides were filtered and collected. The dried transition metal precursors were mixed with a stoichiometric amount of  $\text{LiOH} \cdot \text{H}_2\text{O}$  corresponding to the amount of  $\text{M}(\text{OH})_2$  from the coprecipitation step. Pellets were placed into a furnace at  $480^\circ\text{C}$  for 12 h then sintered at  $1000^\circ\text{C}$  for 12 h in air.

Plastic-like peelable cathode electrodes were designed for use in the *in situ* electrochemical experiment. 51.6 wt.% active material is intimately mixed with 31.8 wt.% polyvinyl difluoride (PVDF) and 16.6 wt.% acetylene black. This mixture was added to an adequate amount of acetone to sufficiently dissolve the polymer and make a uniform slurry. The slurry was then tape cast onto a sheet of Mylar film to obtain an even thickness of 0.66 mm. Following acetone evaporation, the films were peeled off of the sheet and punched into circular disks with a diameter of 12 mm. The punched electrode disks were dried at  $80^\circ\text{C}$  in vacuum overnight.

### 2.2. In situ electrochemical X-ray diffraction

*In situ* XRD of the electrochemical cells was performed using an INEL CPS120 diffractometer (INEL) in reflection geometry. The diffractometer is equipped with a curved position sensitive (CPS) detector, a Cu X-ray tube source, and multilayer mirror optics for increased incident intensity. A Bio-Logic SP-150 potentiostat was used to electrochemically cycle the cell under constant charge and discharge currents corresponding to a rate of C/50 between the desired potential limits 2.25 V and 4.85 V. An XRD pattern was measured every 7 min equivalent to 0.5 mAh/g during electrochemical cycling.

The *in situ* electrochemical cell was assembled in an argon glovebox with a lithium metal anode, a Celgard model C480 separator (Celgard Inc, USA) and a 1 M  $\text{LiPF}_6$  in a 1:1 volume ratio of ethylene carbonate to dimethyl carbonate (Ferro) electrolyte. The cathode and separator were pre-soaked in electrolyte to eliminate excess liquid in the cell to maximize X-ray diffraction signals. The positive current collector of a standard 2032 coin cell was punched with a 9.5 mm diameter hole window for the *in situ* electrochemical measurements. A 0.03 mm thick sheet of Kapton film was adhered over the window using Loctite 11C Hysol Resin and Loctite EPKC Hysol hardener and dried in air at  $60^\circ\text{C}$  overnight. A spring washer was added between the cathode and the positive current collector of the coin cell to prevent direct contact with the Kapton film and establish electrical contact.

### 2.3. Ex situ TEM

Electron microscopy work was carried out on a Cs-corrected FEI Titan 80/300-kV TEM/STEM microscope equipped with a Gatan Image Filter Quantum-865. All STEM images were acquired at 300kV and with a beam size of  $\sim 0.7 \text{ \AA}$ . HAADF images are obtained with a convergence angle of 30 mrad and a large inner collection angle of 65 mrad. To minimize possible electron beam irradiation effects, HAADF figures here are acquired from areas without pre-beam irradiation.

## 3. Results and discussions

### 3.1. In-situ X-ray diffraction

To elucidate when changes in the  $\text{Li}[\text{Li}_{0.2}\text{Ni}_{0.2}\text{Mn}_{0.6}]\text{O}_2$  structure occur during the first electrochemical cycle, *in situ* X-ray diffraction

(XRD) experiments are carried out under constant current charge/discharge. The electrochemical properties as well as the structural parameters of the as-synthesized material have been characterized and the results are reported elsewhere [13]. The electrochemical properties of the *in situ* cell compare favorably to a coin cell prepared without a Kapton window (standard configuration) displaying the characteristic sloping region up to 4.45 V, a plateau region at 4.5 V and a charging capacity exceeding 250 mAh/g. Upon discharge, a large polarization was observed in the *in situ* cell; therefore the discharge capacity achieved was 155 mAh/g instead of the 200 mAh/g capacity in a standard coin cell [8,13]. The electrochemical data presented in this study is represented as voltage versus time to correlate with the time resolved XRD patterns. The cell was cycled with a constant current corresponding to a C/50 rate between 2.25 V and 4.85 V.

Fig. 1 shows several specific XRD peaks evolution versus time. The electrolyte present in the cell reduced the beam intensity, increased background intensities at low angles, and caused overlapping XRD peak positions. Therefore, low angle peaks were not used for quantitative analysis in the present study. Peaks were fit using a Pearson VII type profile shape function and the  $2\theta$  peak center positions are shown versus time in Fig. 1. The decrease in intensity during the discharge region originates from electrolyte interfering with the beam and does not originate from changes in the material. Fig. 2 shows the changes in lattice parameters calculated with Rietveld refinement using Fullprof software [17] during the first electrochemical cycle. The *c* lattice parameter increases during the sloping region, then decreases dramatically during the plateau region. During discharge, the lattice parameters increase to values larger than observed in the

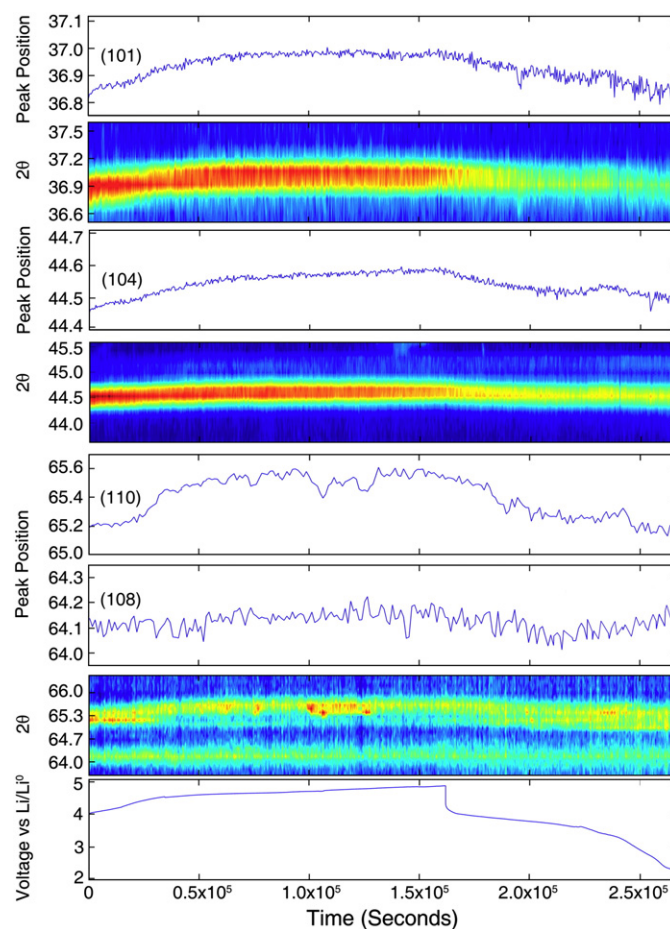
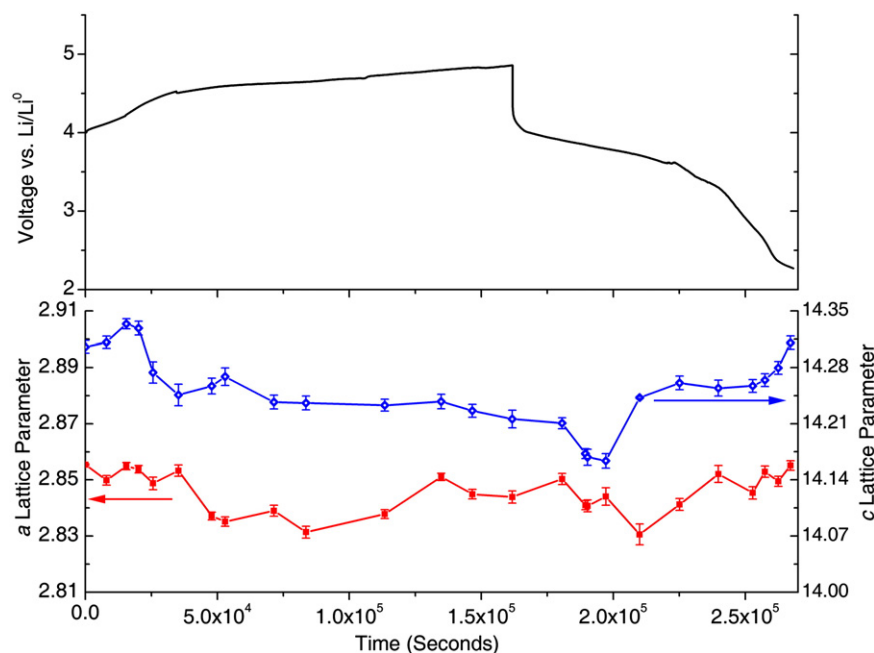


Fig. 1. *In situ* electrochemical measurements during the first charge and discharge cycle with sectioned surface contour plots of the (101), (104), (110) and (108) X-ray diffraction reflections.



**Fig. 2.** The first cycle *in situ* electrochemical profile plotted versus time. Lattice constants  $a$  and  $c$  of  $\text{Li}[\text{Li}_{0.2}\text{Ni}_{0.2}\text{Mn}_{0.6}]\text{O}_2$  plotted as a function of time. The red square and blue diamond lines represent the  $a$  and  $c$  lattice parameters of the pristine material respectively. Error bars shown correspond to  $\sigma$ . (For interpretation of the references to color in this figure legend, the reader is referred to the web version of this article.)

pristine material. These results follow the same trends of previously published literature [2]. Returning to Fig. 1, the peak positions for the (101), (104) and (110) peaks increase monotonically during the sloping region to 4.50 V corresponding to the  $\text{Ni}^{2+}/\text{Ni}^{4+}$  redox region [6]. As  $\text{Li}^+$  is being removed from the layered structure, Ni ions oxidize from  $\text{Ni}^{2+}$  to  $\text{Ni}^{4+}$ , during which the ionic radius decreases from 0.69 Å to 0.48 Å [18]. During this region the material behaves like a solid solution as  $\text{Li}^+$  is removed from  $\text{Li}_{1.2-x}\text{Ni}_{0.2}\text{Mn}_{0.6}\text{O}_2$  based on steady monotonic increases in peak position. Once the electrochemical profile reaches the plateau, the magnitude of the peak position shifts becomes minimal and remains at the largest  $2\theta$  values. The three peaks of (101), (104) and (110) increase by  $0.18^\circ$ ,  $0.14^\circ$  and  $0.35^\circ$  respectively during the sloping region and only increase  $0.05^\circ$  during the plateau region to their maximum values when the corresponding charging capacity reaches 200 mAh/g. The material does not show evidence of degradation of the pristine phase during the first charging step. Upon discharge the (101), (104) and (110) peak positions consistently decrease in their  $2\theta$  position, though do not return to the original positions. The  $c$  lattice parameter increases from a minimum value of 14.169 Å at the end of the first charge to 14.311 Å after the first discharge. Similarly, the  $a$  lattice parameter increases from 2.840 Å at the end of the first charge to 2.855 Å following discharge. The fully discharged material loses 100 mAh/g capacity which corresponds to approximately 0.27 mol of  $\text{Li}^+$  irreversibly lost from first discharge. Irreversible capacities previously reported range between 50 and 100 mAh/g in this material [5,13], which is in good agreement to that observed in the current study. The final shifts in peak positions are consistent with the permanent changes to the crystal structure resulting from dynamic cation migration during electrochemical cycling. The permanent shifts in the peak positions support previously reported results that the superstructure peaks dramatically decrease following electrochemical cycling and the  $c/a$  lattice ratio expands [12,13].

During the first electrochemical cycle, the (108) plane remains unchanged and predominantly corresponds to the out-of-plane ordering, which intersects 1 in every 8 transition metal (TM) or  $\text{Li}^+$  layers (along the  $c_{\text{hex}}$  axis) as seen in Fig. 3a. The out-of-plane ordering shows changes corresponding strongly to the  $c$  lattice parameter.

As  $l$  increases in the (10 $l$ ) family of peaks, the two theta peak position shift decreases in magnitude. Fig. 3b shows the (110) plane illustrating the in-plane slice corresponding to the  $\sqrt{3}a_{\text{hex}} \times \sqrt{3}a_{\text{hex}}$  ordering in the TM layers as well as faults in the stacking sequences perpendicular to the TM layers along the  $c_{\text{hex}}$  axis [1]. A sharp increase in the  $2\theta$  position of the (110) peak strongly correlates with decreases in the  $a$  lattice parameter illustrating strong anisotropy in the material during the charging step. The degree of  $2\theta$  separation (110) and (108) peaks has been previously associated with the layeredness and ordering in the material. At the end of the plateau region, the difference in  $2\theta$  positions of these two peaks is the greatest.

### 3.2. Strain effects during electrochemical cycling

Evidence for microstrain can be extracted by examining line broadening observed in the XRD patterns. With a technique developed by Williamson and Hall [19], X-ray line broadening can be used to determine microstrain and crystallite size in a given sample.

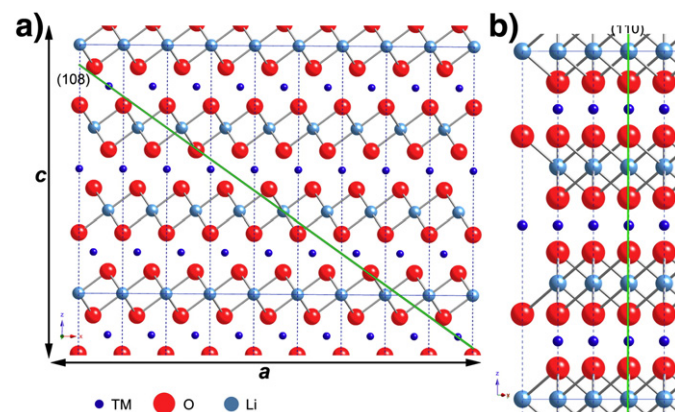


**Fig. 3.** The a) (108) and b) (110) planes through the representative structure of the  $\text{Li}[\text{Li}_{0.2}\text{Ni}_{0.2}\text{Mn}_{0.6}]\text{O}_2$  illustrating alternating transition metal, oxygen and lithium layers.

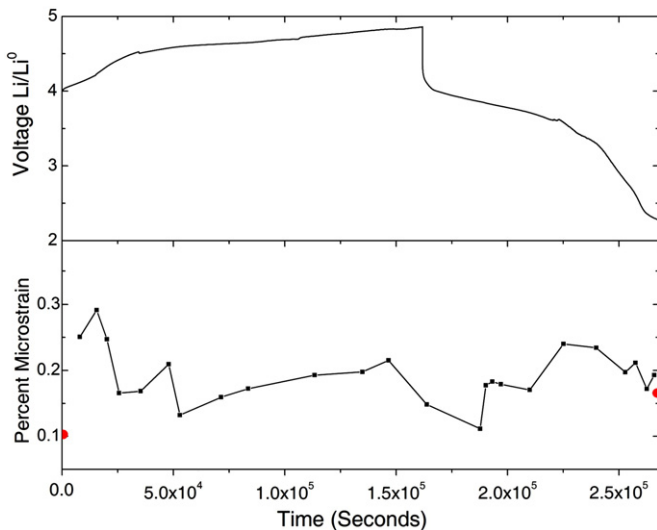


**Fig. 4.** *In situ* electrochemical measurements combined with the strain calculated using Williamson–Hall equations during electrochemical cycling. Red dots correspond to strain measurements obtained from the as-synthesized ( $t=0$ ) and *ex situ* measurement ( $t=2.68 \times 10^5$ ). (For interpretation of the references to color in this figure legend, the reader is referred to the web version of this article.)

The Williamson–Hall method considers the contributions of particle size and strain in X-ray line broadening to be additive.

$$\beta_{\text{total}} = \beta_{\text{particle size}} + \beta_{\text{strain}} \quad (1)$$

Broadening due to small particle size is given by the Scherrer equation while the contribution of broadening due to strain is obtained by differentiating the Bragg law [20].

$$\beta_{\text{total}} = \frac{0.94\lambda}{t \cos\theta} + 4 \tan\theta \left( \frac{\Delta d}{d} \right) \quad (2)$$

Multiplying both sides of Eq. 2 by  $\cos\theta$  gives the final form.

$$\beta_{\text{total}} \cos\theta = \frac{0.94\lambda}{t} + 4 \tan\theta \left( \frac{\Delta d}{d} \right) \quad (3)$$

The diffraction angle is given by  $\theta$ ,  $\beta_{\text{total}}$  is calculated from the measured FWHM (in radians),  $\lambda$  is the X-ray wavelength of the source ( $\text{Cu K}\alpha = 0.154 \text{ nm}$ ),  $t$  is the particle size, and the strain is represented by  $\Delta d/d$ . The strain is extracted from the slope of the plot of  $\beta \cos\theta$  versus  $4 \sin\theta$ . The microstrain extracted from Williamson–

Hall type analysis can be explained by non-uniform strain originating from systematic shifts of atoms from their ideal positions resulting from defects such as point defects, site-disorder and vacancies as well as plastic deformation. Fig. 4 shows strain values obtained at different points of the first electrochemical cycle. The points at  $t=0$  and  $t=2.6 \times 10^5 \text{ s}$  correspond to the pristine material and the electrochemically cycled material obtained following 10 cycles, respectively. The plot shows that the strain in the material increases during the initial sloping region.

The combined results allow us to propose a mechanism to explain the changes in strain during the first electrochemical cycle. The increase in strain during the sloping region could be attributed due to the removal of Li from the lithium layer causing a concentration gradient in the structure. As Li is extracted from the lithium layer, strains may originate from electrostatic repulsions from adjacent oxygen layers. Our previous research showed that in this region, the Li migrated into the tetrahedral sites above and below the Li layer [21]. Preliminary research suggests that  $\text{Ni}^{2+}$  ions may migrate to adjacent Li layer causing site vacancies in the TM layer. Moreover the Li transport is accompanied by the oxidation of  $\text{Ni}^{2+}$  to  $\text{Ni}^{4+}$  which could impart stress on the structure due to the shrinking  $a$  lattice parameters. The lithium ions can form an energetically stable phase with tetrahedral dumbbells by the end of the slope region and at the same time the lithium layer will be partially filled by migrating Ni ions mitigating the strain created by local lithium concentration gradient. This reduces the microstrain as observed at the beginning of the plateau region. During the plateau region, the strain begins to increase. There are several mechanisms that could explain this increase in strain. First, previous research has indicated oxygen removal occurs during the plateau [5,9,11]. The Li ions in the TM layer are removed simultaneously with oxygen loss. A second possibility is that lithium and oxygen vacancies are created *non-uniformly* during the plateau region, which may increase microstrain in the structure. Fig. 6a shows *ex situ* TEM taken at this plateau region. The figure depicts changes in image contrast indicating the material is full of defects and strain.

As the discharge step begins, the strain decreases first then increases to a value matching that observed from *ex situ* measurements. This validates the results found by the present *in situ* study. The reduction in strain at the beginning of the discharge cannot be clearly explained yet. Overall, during the discharge step, the strain increases. This originates from the large  $\text{Li}^+$  ions re-entering the structure causing lattice expansion and filling lattice vacancies. During the charging step, the material has a clear strain and stress relief mechanism via lithium tetrahedral formation, oxygen loss and transition metal migration; however, during discharge, these mechanisms are no longer available. Fig. 5b shows an *ex situ* HAADF-TEM image taken after the

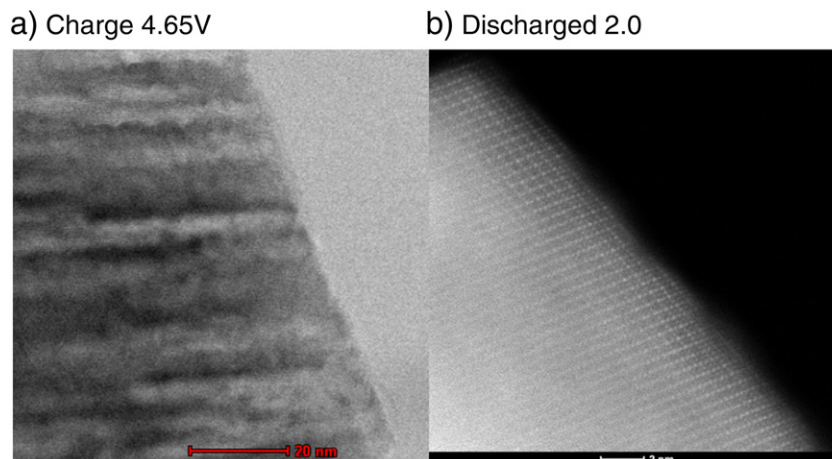


**Fig. 5.** *Ex situ* S/TEM and HAADF images of the bulk and surface region of  $\text{Li}[\text{Li}_{0.2}\text{Ni}_{0.2}\text{Mn}_{0.6}]\text{O}_2$  a) charged to 4.65 V and b) following one electrochemical charge/discharge cycle.

first electrochemical discharge cycle. The image reveals that the surface loses faceting and a second crystal structure phase forms at the surface. Our previous findings indicate that the energetically stable defect-like spinel phase forms at the end of the first electrochemical cycle [21]. Second phase particles and concentration gradients in the particles both contribute to non-uniform microstrain.

The proposed lithium and transition metal migration mechanisms are depicted in Fig. 6. The first electrochemical cycle is divided into 7

regions. Initially Li ions are removed from the Li layer causing a concentration gradient and electrostatic repulsion from adjacent oxygen layers accounting for the increased strain and  $c$  lattice parameters (Fig. 6b). At the end of the sloping region (Fig. 6c), Ni and Mn ions are in their fully oxidized 4+ state. Our previous finding [21] indicates that energetically stable tetrahedral Li ions form. These two factors account for the  $a$  and  $c$  lattice collapse and the strain decreases at the end of the sloping region. During region 4 (Fig. 6d), the plateau region,  $a$  lattice parameter

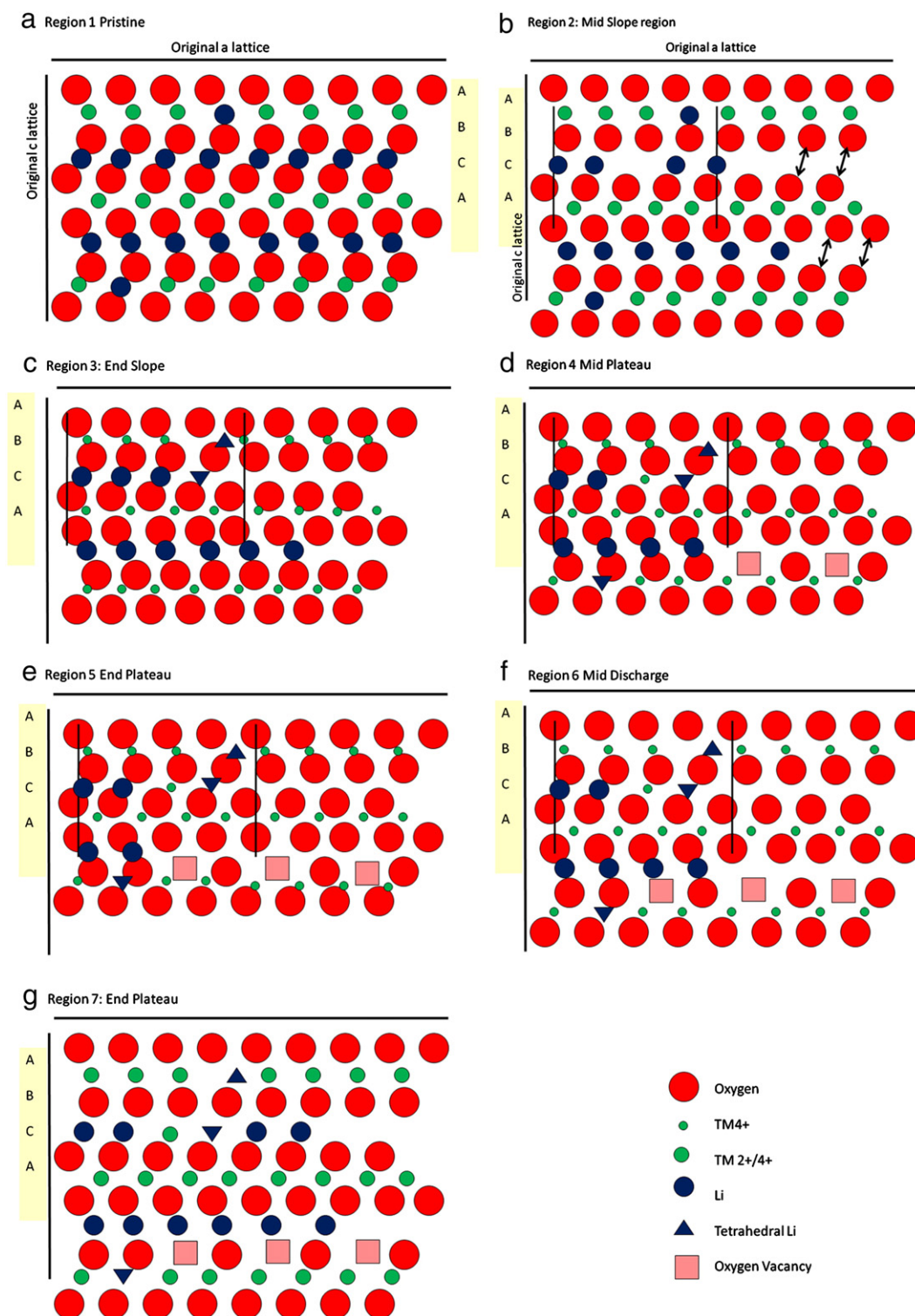


**Fig. 6.** Sketch of Li and TM cation migration during 7 regions (a–g) of the first electrochemical charge/discharge cycle. (Red: oxygen, green: TM, blue: Li, pink: vacancy). (For interpretation of the references to color in this figure legend, the reader is referred to the web version of this article.)

increases while  $c$  lattice parameter continues to decrease while the strain increases. This indicates that the strain can be correlated to the  $a$  lattice changes. During the plateau region, simultaneous oxygen and Li removal creates large vacancies across several layers. Transition metal cations may migrate to fill these large vacancies causing the  $c$  lattice parameter to remain stable; however, the increase in  $a$  lattice parameter may be attributed to new electrostatic repulsion forces. The first source may originate from an unbalanced number of oxygen in the cation octahedrals due to oxygen vacancies. The second source of electrostatic repulsion may originate from adjacent oxygen ions near vacant oxygen sites. The TEM images, (Fig. 5a), from this region confirm the large strains and high density of defects throughout the particles. As large Li ions are reinserted into the structure during the discharge step as seen in Fig. 6g, both lattice parameters and the strain begin to increase. The material no longer has TM migration and second phase formation to mitigate the strain formation. During the final discharge step (Fig. 6f), the material has expanded in volume compared to the original structure.

During the first electrochemical cycle, the material undergoes large changes in strain; however is able to reversibly cycle well with little capacity loss indicating that this lithium excess family of materials can structurally withstand large lattice dimension changes (strain). Our *in situ* analysis of specific structural changes in  $\text{Li}[\text{Li}_{0.2}\text{Ni}_{0.2}\text{Mn}_{0.6}]\text{O}_2$  material shed some light in understanding the dynamic changes happening in these complex oxides when Li is extracted and/or inserted. The observed changes in the lattice parameters and strain and their relations to the electro-mechanical properties of layered lithium excess oxides deserve more in-depth studies.

#### 4. Conclusions

*In situ* X-ray diffraction of the lithium excess layered oxide compound,  $\text{Li}[\text{Li}_{0.2}\text{Ni}_{0.2}\text{Mn}_{0.6}]\text{O}_2$ , during electrochemical cycling has been studied using a laboratory diffractometer. The data provides evidence that the structure undergoes irreversible changes in lattice parameters and strain during the first electrochemical cycle. Rietveld refinement of the X-ray diffraction data of the electrochemically cycled electrode materials shows dynamically changing lattice parameters. Anisotropy in  $a$  and  $c$  directions is observed and is the greatest during the plateau region. Following the electrochemical cycling, both lattice parameters have expanded from the pristine material showing irreversible changes. Microstrains observed in the material were extracted using Williamson–Hall analysis. The strain analysis shows that the material undergoes large changes in the strain; however is able to reversibly cycle. During the charging cycle, the charge compensation mechanisms such as oxygen removal and cation migration accommodate the strain; however during discharge, these compensation mechanisms

do not exist; therefore, causing the strain to increase. The large changes in strain are linked to the lithium and cation transport mechanisms observed in these materials.

#### Acknowledgments

J.L Jones acknowledges the financial support from the National Science Foundation through award DMR-0746902. Y.S. Meng acknowledges the financial support from the Northeastern Center for Chemical Energy Storage (NECCES), an Energy Frontier Research Center funded by the U.S. Department of Energy, Office of Science, Office of Basic Energy Sciences under Award Number DE-SC 0001294. a-S/TEM analysis is carried out at the ORNL Shared Research Equipment (SHaRE) User Facility, which is sponsored by the Office of Basic Energy Sciences, U.S. Department of Energy. C. R. Fell acknowledges the financial support from Florida Energy System Consortium through University of Florida under Award Number 80859. C. R. Fell would like to acknowledge the assistance from A. Emly and M. Yang and B. Xu.

#### References

- [1] Y.S. Meng, G. Ceder, C.P. Grey, W.S. Yoon, M. Jiang, J. Breger, Y. Shao-Horn, *Chem. Mater.* 17 (9) (2005) 2386.
- [2] Z. Lu, J.R. Dahn, *J. Electrochem. Soc.* 149 (7) (2002) A815.
- [3] V. Massarotti, M. Bini, D. Capsoni, A. Altomare, A.G.G. Moliterni, *J. Appl. Crystallogr.* 30 (1997) 123.
- [4] P. Strobel, B. Lambert-Andron, *J. Solid State Chem.* 75 (1) (1988) 90.
- [5] Z. Lu, D.D. MacNeil, J.R. Dahn, *Electrochem. Solid-State Lett.* 4 (11) (2001) A191.
- [6] W.S. Yoon, Y. Paik, X.Q. Yang, M. Balasubramanian, J. McBreen, C.P. Grey, *Electrochem. Solid-State Lett.* 5 (11) (2002) A263.
- [7] W.S. Yoon, C.P. Grey, M. Balasubramanian, X.Q. Yang, J. McBreen, *Chem. Mater.* 15 (16) (2003) 3161.
- [8] Z. Lu, L.Y. Beaulieu, R.A. Donaberger, C.L. Thomas, J.R. Dahn, *J. Electrochem. Soc.* 149 (6) (2002) A778.
- [9] A.D. Robertson, P.G. Bruce, *Electrochem. Solid-State Lett.* 7 (9) (2004) A294.
- [10] C.P. Grey, W.S. Yoon, J. Reed, G. Ceder, *Electrochem. Solid-State Lett.* 7 (9) (2004) A290.
- [11] A.R. Armstrong, M. Holzappel, P. Novak, C.S. Johnson, S.H. Kang, M.M. Thackeray, P.G. Bruce, *J. Am. Chem. Soc.* 128 (26) (2006) 8694.
- [12] M. Jiang, B. Key, Y.S. Meng, C.P. Grey, *Chem. Mater.* 21 (13) (2009) 2733.
- [13] C.R. Fell, K.J. Carroll, M. Chi, Y.S. Meng, *J. Electrochem. Soc.* 157 (11) (2010) A1202.
- [14] M.N. Richard, I. Koetschau, J.R. Dahn, *J. Electrochem. Soc.* 144 (2) (1997) 554.
- [15] M.R. Palacín, F. Le Cras, L. Seguin, M. Anne, Y. Chabre, J.M. Tarascon, G. Amatucci, G. Vaughan, P. Strobel, *J. Solid State Chem.* 144 (2) (1999) 361.
- [16] M. Morcrette, Y. Chabre, G. Vaughan, G. Amatucci, J.B. Leriche, S. Patoux, C. Masquelier, J.M. Tarascon, *Electrochim. Acta* 47 (19) (2002) 3137.
- [17] J. Rodríguez-Carvajal, Satellite Meeting on Powder Diffraction of the XV Congress of the IUCr, Toulouse, France, 1990.
- [18] R.D. Shannon, C.T. Prewitt, *Acta Crystallogr.* B25 (1969) 925.
- [19] G.K. Williamson, W.H. Hall, *Acta Metall.* 1 (1) (1953) 22.
- [20] B.D. Cullity, S.R. Stock, *Elements of X-ray Diffraction*, 3rd ed, Prentice Hall, 2001.
- [21] B. Xu, C.R. Fell, M. Chi, Y.S. Meng, *Energy Environ. Sci.* 4 (6) (2011) 2223.